4-29-2014

Crustal Velocity Structure of the Northeastern Tibetan Plateau from Ambient Noise Surface-Wave Tomography and its Tectonic Implications

Xinfu Li

Hongyi Li

Yang Shen
University of Rhode Island, y.shen@icloud.com

Meng Gong

Danian Shi

See next page for additional authors

Citation/Publisher Attribution

Crustal Velocity Structure of the Northeastern Tibetan Plateau from Ambient Noise Surface-Wave Tomography and its Tectonic Implications

Authors
Xinfu Li, Hongyi Li, Yang Shen, Meng Gong, Danian Shi, Eric Sandvol, and Aibing Li

Ⓔ

Crustal Velocity Structure of the Northeastern Tibetan Plateau from Ambient Noise Surface-Wave Tomography and Its Tectonic Implications

by Xinfu Li,[*] Hongyi Li,[*] Yang Shen, Meng Gong, Danian Shi, Eric Sandvol, and Aibing Li

Abstract   Broadband seismic data from the regional seismic network operated by the China Earthquake Administration and 32 temporary seismic stations are used to image the crustal velocity structure in the northeast Tibetan plateau. Empirical Rayleigh- and Love-wave Green's functions are obtained from interstation cross correlation of continuous seismic records. Group velocity dispersion curves for Rayleigh and Love waves between 10 and 50 s are obtained using the multiple-filter analysis method with phase-matched processing. The group velocity variations of Rayleigh and Love waves overall correlate well with the major geologic structures and tectonic units in the study region. Shear-wave velocity structures were then inverted from Rayleigh- and Love-wave dispersion maps. The results show that the Songpan–Ganzi terrane is associated with a low velocity at depth greater than 20 km. The northern Qilian orogen, with higher elevation and thicker crust compared to the southern Qilian orogen, is also dominated by low velocity at depth greater than ∼25 km. However, there is no clear evidence of the low-velocity mid-to-lower crust beneath the southern Qilian orogen as the crustal flow model predicts. The low-velocity zone (LVZ) beneath the northern Qilian orogen may suggest that the crustal thickening and surface uplift of the northern Qilian orogen are related to the LVZ, and the LVZ may be considered as an intracrustal response to bear the ongoing deformation in the northern Qilian orogen.

Online Material: Figures of crustal topography, number of group velocity measurements, checkerboard tests for NETS stations, and 1D velocity models.

Introduction

The Tibetan plateau has been the prime site for understanding the processes of continental collision, mountain building, and the interaction between tectonics and climate change. The collision between the Indian and Eurasian plates not only has caused significant elevation and highly deformed orogenic belts within the Tibetan plateau, but also impacts remote areas such as eastern China and the Baikal rift to the north (Molnar and Tapponnier, 1975; Tapponnier and Molnar, 1977; Bendick and Flesch, 2007). Many studies have been performed in the Tibetan plateau, but most of the geophysical studies of the Tibetan crust and mantle structure to date have focused on the southern (Brown *et al.*, 1996; Kind *et al.*, 1996; Nelson *et al.*, 1996; Huang *et al.*, 2000; Wei *et al.*, 2001; Wang *et al.*, 2003; Unsworth *et al.*, 2005; Yao *et al.*, 2008; Guo *et al.*, 2009), central (Owens and Zandt, 1997; Kind *et al.*, 2002; Tilmann *et al.*, 2003), and eastern Tibetan plateau (Li *et al.*, 2009), with the primary objectives of understanding the continental collision process and the intrusion of the crustal and mantle materials from the Indian plate into the Eurasian plate. In comparison to other parts of the plateau, fewer seismic investigations have been done in the northeastern Tibetan plateau (e.g., Wittlinger *et al.*, 1996; Zhu and Helmberger, 1998; Vergne *et al.*, 2002, 2003; Karplus *et al.*, 2011, 2013; Yue *et al.*, 2012), which either are localized along linear profiles or focused on the velocity discontinuity structure. In our previous study (Li *et al.*, 2012), we determined that the low-velocity zone (LVZ) terminated around the east Kunlun fault (KLF) in the northeastern Tibetan plateau. However, due to the coarse resolution (1.6°) and lack of data (we only used data from the China Provincial Digital Seismic Networks, Kyrgyzstan network, and Kazakhstan network), we did not resolve any features in the Qilian orogen. In this study, we complemented the data from the China Earthquake Networks Center with the northeastern Tibet seismic experiment (Shen *et al.*, 2008). These additional broadband, passive-source seismic

---

*Also at School of Geophysics and Information Technology, China University of Geosciences, Beijing, 100083, China.
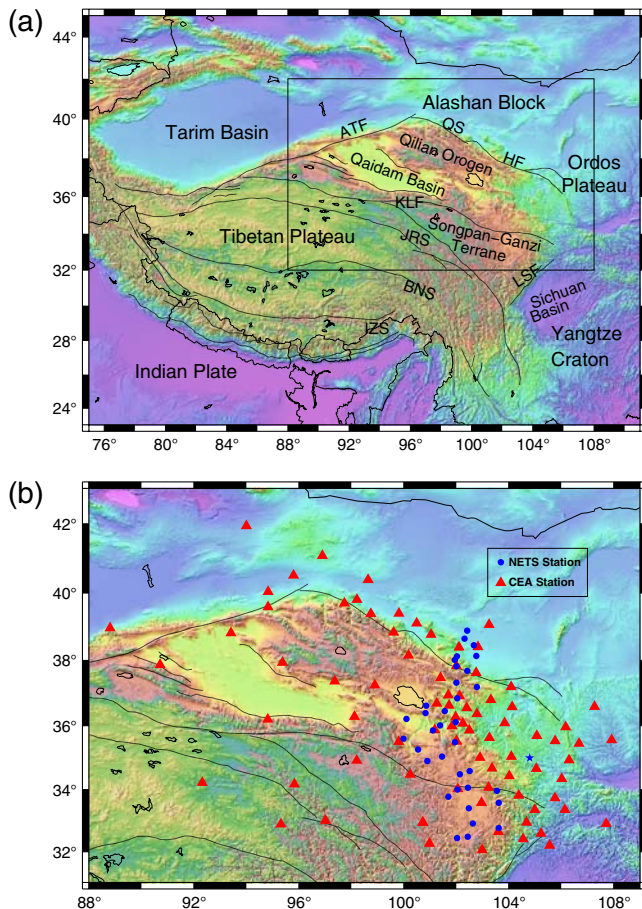
Figure 1. (a) Topographic relief of the Tibetan plateau and adjacent areas and (b) the distribution of seismic stations used in this study. Dashed lines mark tectonic elements. The rectangle in (a) indicates the study area. ATF, Altyn-Tagh Fault; QS, Qinling Suture; HF, Haiyuan Fault; KLF, KunLun Fault; JRS, Jinsha–River Suture; BNS, Bangong–Nujiang Suture. In (b), the triangles are seismic stations belonging to the Seismic Network of Gansu Province and the Chinese center of Digital Seismic Network (CCDSN). The solid circles are the stations of northeast Tibet seismic (NETS) array from June 2008 to July 2010. The star denotes the location referred to in Figure 7. The color version of this figure is available only in the electronic edition.

experiments were designed to investigate the lithospheric structure and evolution of the northeastern Tibetan plateau (Fig. 1) and contributed additional high-quality data to resolve the structure under the northeastern portion of the Tibetan plateau.

The deformation process of the Tibetan plateau is generally attributed to a series of collision events (Molnar *et al.*, 1993; Owens and Zandt, 1997; Tapponnier *et al.*, 2001; Chung *et al.*, 2005; Dai *et al.*, 2011). The deformation mechanism of the Tibetan plateau and its adjacent regions may be characterized by several models of collision between India and Eurasia, such as a unidirectional underthrust model and bidirectional subduction model. In the unidirectional underthrust model, the Indian lithosphere subducts northward, the Songpan–Ganzi oceanic lithosphere was subducted northward beneath the Kunlun blocks (Powell and Conaghan, 1975; Molnar *et al.*, 1993; Yin and Harrison, 2000),

and the Qaidam basin acted as an obstacle (Zhao and Morgan, 1985; Yin and Harrison, 2000). In the bidirectional subduction model, in addition to this northward subduction, the Tarim basin and the Qaidam basin lithospheres are being subducted southward (Pearce and Mei, 1988; Arnaud *et al.*, 1992; Xu, 1992; Deng, 1997; Tapponnier *et al.*, 2001; Kind *et al.*, 2002; C. Zhang *et al.*, 2010; Z. Zhang *et al.*, 2010; Q. Zhang *et al.*, 2011; Z. Zhang *et al.*, 2011). Aside from these two models, some studies suggest that the stronger Indian plate is embedded in the Tibetan plateau and the force of collision leads to the lateral escape of the plateau materials toward the southeast and the east along a series of strike-slip faults (e.g., Molnar and Tapponnier, 1975; Tapponnier and Molnar, 1977). Tapponnier *et al.* (2001) suggested an oblique crustal subduction accommodated by the extrusion tectonics to be the mechanism of the growth and uplift of the eastern Tibetan plateau. However, other researchers (e.g., Royden *et al.*, 1997, 2008; Clark and Royden, 2000; Clark *et al.*, 2005) consider that the lower crustal flow may be responsible for the different topographic profiles at the different margins of the Tibetan plateau. Low-velocity and low-resistivity materials have been observed beneath the eastern Tibetan plateau (Li *et al.*, 2009; Bai *et al.*, 2010), but geophysical evidence of the proposed flow paths remains to be found in the northeast Tibetan plateau.

In this study, we focus on a complex junction that connects the margin of the Tibetan plateau with the Tarim basin, Sichuan basin, Ordos plateau, and Alashan block (Fig. 1), where 32 temporary broadband stations were deployed between June 2008 and July 2010 (Shen *et al.*, 2008). Our study area contains the northeast Tibetan plateau, the Songpan–Ganzi terrane, the Qilian orogen, and the Alashan block, which are separated by the Haiyuan fault (HF) system and Qinling suture (QS) in the north and the KLF system and the Qaidam basin in the south (Fig. 1). The convergence in the northeast Tibetan plateau has been accommodated by the left lateral strike-slip motion (with a slip rate of ~12 mm/yr) along the KLF (e.g., Tapponnier *et al.*, 2001; Wang *et al.*, 2001; Zhang *et al.*, 2004). Therefore, this region is very suitable to study the mechanisms responsible for the rising of the Tibetan plateau and the role of the KLF in accommodating the convergence of the India–Asia collision.

In this article, we apply the ambient noise method to the northeastern Tibetan plateau to obtain a high-resolution crustal velocity structure. Three-component time series, recorded at 81 broadband stations of Provincial Digital Seismic Networks and 32 broadband stations deployed by China University of Geosciences in Beijing, Chinese Academy of Geological Sciences, University of Rhode Island, University of Houston, and University of Missouri between June 2008 and July 2010, are cross correlated to estimate both Rayleigh- and Love-wave Green's functions. The resulting group velocity maps have resolutions on the order of ~100 km in most parts of the northeast Tibetan plateau and generally show good correlations with major geologic and tectonic units in the study region. We invert shear-wave velocity
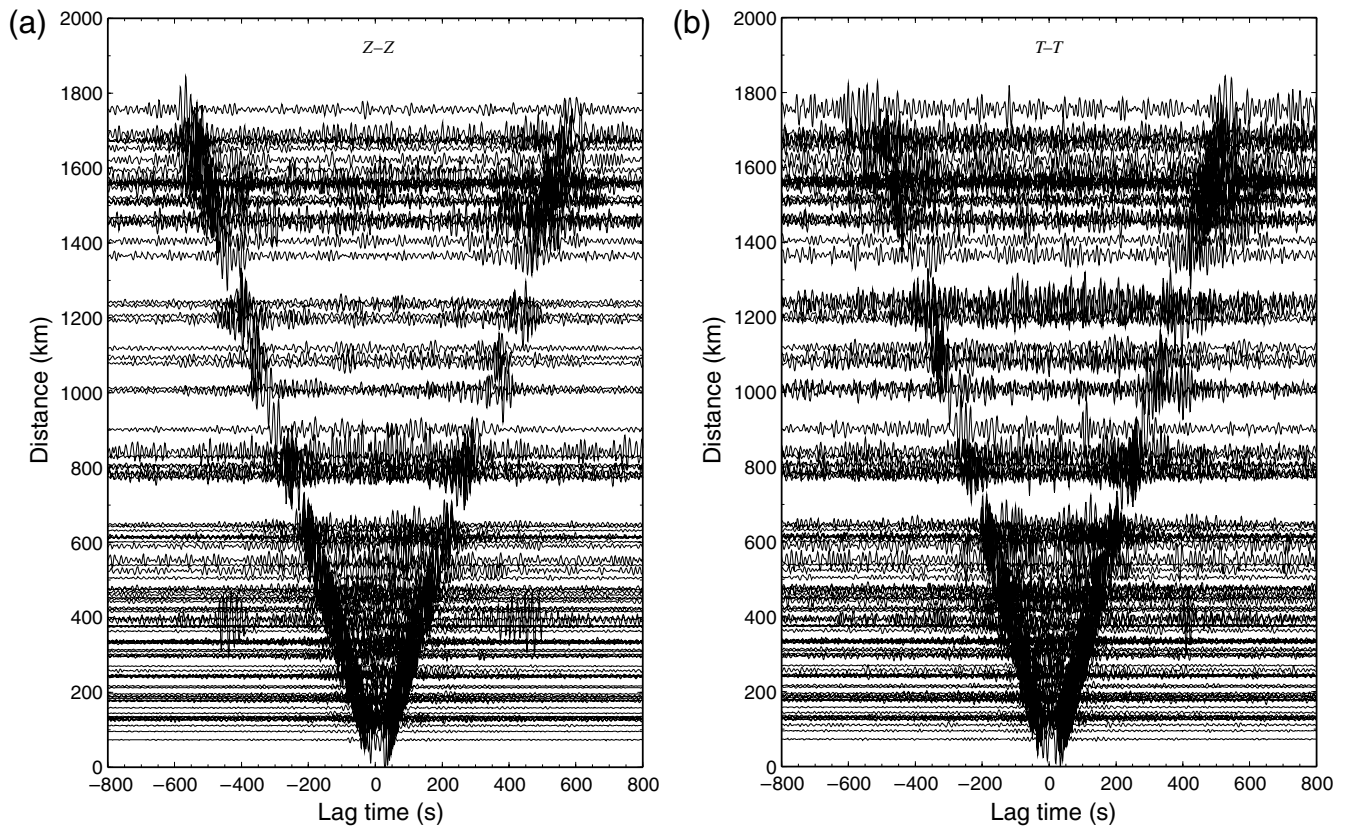
Figure 2.   The 10–100 s band-pass filtered cross-correlation record section centered at station ZEKU with (a) vertical–vertical (Z−Z) cross correlations and (b) transverse–transverse (T−T) cross correlations.

structures from Rayleigh- and Love-wave group velocities and discuss their geologic and tectonic implications.

Data Selection and Processing

In this study, we collected continuous three-component broadband seismic data recorded at 81 regional stations from the China Earthquake Networks Center between January 2008 and September 2009 and 32 temporary stations from June 2008 to July 2010. We followed the same ambient noise cross-correlation processing procedure as described in our previous studies (Li *et al.*, 2009; Li, Bernardi, and Michelini, 2010; Li, Su, *et al.*, 2010; Li *et al.*, 2012). The data were first windowed into one-hour-long time series, after removing trend, mean value, and instrument response. The north–south and east–west components were then rotated to the radial and transverse components for each station pair by setting the first station as the event and the second station as the receiver before the cross correlations are calculated and stacked. Next, each stacked cross correlation was cut into positive and negative lags, and the two correlation lags were added together to produce the final cross-correlation function.

Figure 2 shows record sections of cross correlations between station ZEKU and other stations for the Rayleigh wave (Z−Z; Fig. 2a) and the Love wave (T−T; Fig. 2b), respectively. As seen in Figure 2, clear signals simultaneously emerge at both positive and negative correlation lags for Rayleigh and Love waves, and Rayleigh waves generally display a higher signal-to-noise ratio than Love waves. Then the group velocity dispersion measurement was performed based on the multiple-filter technique with phase-matched processing (Dziewonski *et al.*, 1969; Herrmann, 1973). The waveforms were first band-pass filtered with the narrowband Gaussian filter operator $\exp[-\alpha(\omega - \omega_0)^2/\omega_0^2]$, in which ω_0 is the central frequency of the desired period and α is a tunable parameter to balance the resolutions in the frequency and time domains and is usually distance dependent. After that, a phase-matched filter was then constructed and performed for the signal to isolate the fundamental mode. We visually checked each dispersion measurement to make sure that only the reliable dispersion curves were selected for our inversion. In this study, we obtained more than 3200 group velocity dispersion curves for Rayleigh waves and about 2000 curves for Love waves.

Figure 3 shows the number of group velocity dispersion measurements for Rayleigh and Love waves at different periods. In this article, only station pairs with the interstation distances larger than three wavelengths of the waves of interest are selected for our inversion. Because of higher noise levels on the horizontal components, fewer interstation paths of Love waves are selected from the cross correlation of the T−T component in comparison with Rayleigh waves from that of Z−Z component. For the Rayleigh-wave tomography,
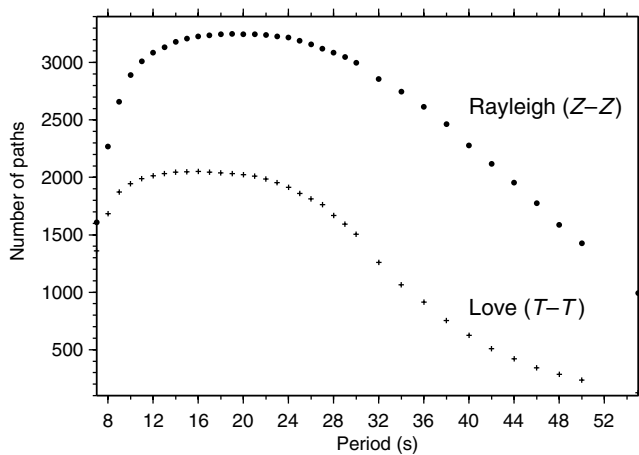
Figure 3.   Number of group velocity dispersion measurements at different periods.

the longest period can extend to about 50 s; however, for the Love-wave tomography at periods longer than 40 s, the station coverage becomes poor for most of the study area except for the southern Qilian orogen.

Group Velocity Tomography

The dispersion measurements from more than 3200 paths were used to invert for group velocity maps at periods from 10 to 50 s for Rayleigh and Love waves. The study area was divided into a $0.4° \times 0.4°$ grid, and the Occam's inversion scheme, which seeks a smooth model that fits the observations (Constable *et al.*, 1987), was adopted for inversion (Constable *et al.*, 1987; DeGroot-Hedlin and Constable, 1990). Before inversion, checkerboard tests were conducted to evaluate lateral resolution with the Occam's inversion technique. Figure 4a shows an input checkerboard velocity model. The size of alternative low- and high-velocity cells is $0.4°$. Alternating positive and negative $\pm 5\%$ velocity perturbations are assigned to each cell, with average velocity of 3.0 km/s. Synthetic group velocity data were calculated according to the actual paths at the 30 s period, and then random errors with a standard deviation of 0.05 km/s were added to each path. Figure 4b and c shows the ray-path density at the 30 s period for Rayleigh and Love waves, respectively. Generally, the coverage is good for the northeastern and southern parts (the Qilian orogen, east KLF, and the south of the Qaidam basin), but in the western part of the study region, the path coverage (and hence resolution) is poor due to few available stations. The checkerboard test results are given in Figure 4d for Rayleigh wave and Figure 4e for Love wave. The reconstructed velocity models are basically correct in most of the study area. The resolving power is generally good in the northeastern and southeastern parts of the study area, but it becomes worse beneath the Qaidam basin where the path coverage is sparse. The lateral resolution is estimated to be $\sim 0.8°$ for both Rayleigh and Love waves in the eastern part of the study area and $1.2°$ for the Rayleigh

wave beneath the Qaidam basin. Surface wave speeds are known to exhibit a frequency-dependent sensitivity to the Earth's structure. In general, the longer the period, the deeper the surface-wave energy penetrates. Because our previous study (Li *et al.*, 2012) gave the radial sensitivity kernels for Rayleigh and Love waves and showed that Rayleigh waves sample down to depths approximately one-third of their wavelength and Love waves are more affected by shallow structures, we do not elaborate here.

The Rayleigh-wave group velocity images at 10, 30, and 50 s are presented in Figure 5. At the short-period range (≤ 20 s) Rayleigh-wave group velocities are most sensitive to shear velocities in the upper crust. In the 10 s period map (Fig. 5a), the prominent low group velocities are clearly observed beneath the Qaidam basin. The surrounding mountain areas show overall higher velocities than the basin at this period. We note a small patch of high velocity in the northern part of the Qilian orogen. At the 30 s period (Fig. 5b), the Qaidam basin is still featured with very low velocity; meanwhile, a very low group velocity anomaly also occurs in the Songpan–Ganzi terrane. We also note that the small patch of high velocity in the northernmost Qilian orogen still exists. In the 50 s map (Fig. 5c), the group velocity distribution is different from those at short-to-intermediate periods, the lowest velocities are observed beneath the Songpan–Ganzi terrane rather than the Qaidam basin. The Love-wave maps at 10 and 30 s (Fig. 6) exhibit similar features to the Rayleigh-wave maps. In the 10 s Love-wave map (Fig. 6a), the low velocity also appears beneath the Qaidam basin, and a small patch of high velocity is observed beneath the northernmost Qilian orogen. In the 30 s map (Fig. 6b), the Qaidam basin and the Songpan–Ganzi terrane still show low velocities. The strong difference in group velocities among the different subregions reveals strong lateral variations in the crust in the northeast Tibetan plateau.

Shear-Wave Velocity Structure

As it is well known that surface waves at different periods are sensitive to the shear-wave velocity structure over different depth ranges, so they can provide useful information to constrain the shear-wave velocity structure and valuable insights into the lateral variation of shear-wave velocities in different depths. We use the pure-path Rayleigh- and Love-wave dispersion curves for each grid node to carry out inversion for the shear-wave velocity structure with a program developed by Herrmann and Ammon (2004). The shear-wave velocity in each layer with fixed thickness is taken as the inversion parameter, and *P*-wave velocity and density are calculated from shear-wave velocity with empirical formulas. The shear-wave velocity and Moho depth in the initial models are referred to the deep seismic sounding profiles (Xu *et al.*, 2002; Zhao *et al.*, 2004; S. Li *et al.*, 2006), tomography results (Huang *et al.*, 2003; Wang *et al.*, 2003, 2007; Maceira *et al.*, 2005), and receiver functions (Pan and Niu, 2011; Ⓔ Fig. S1, available in the electronic
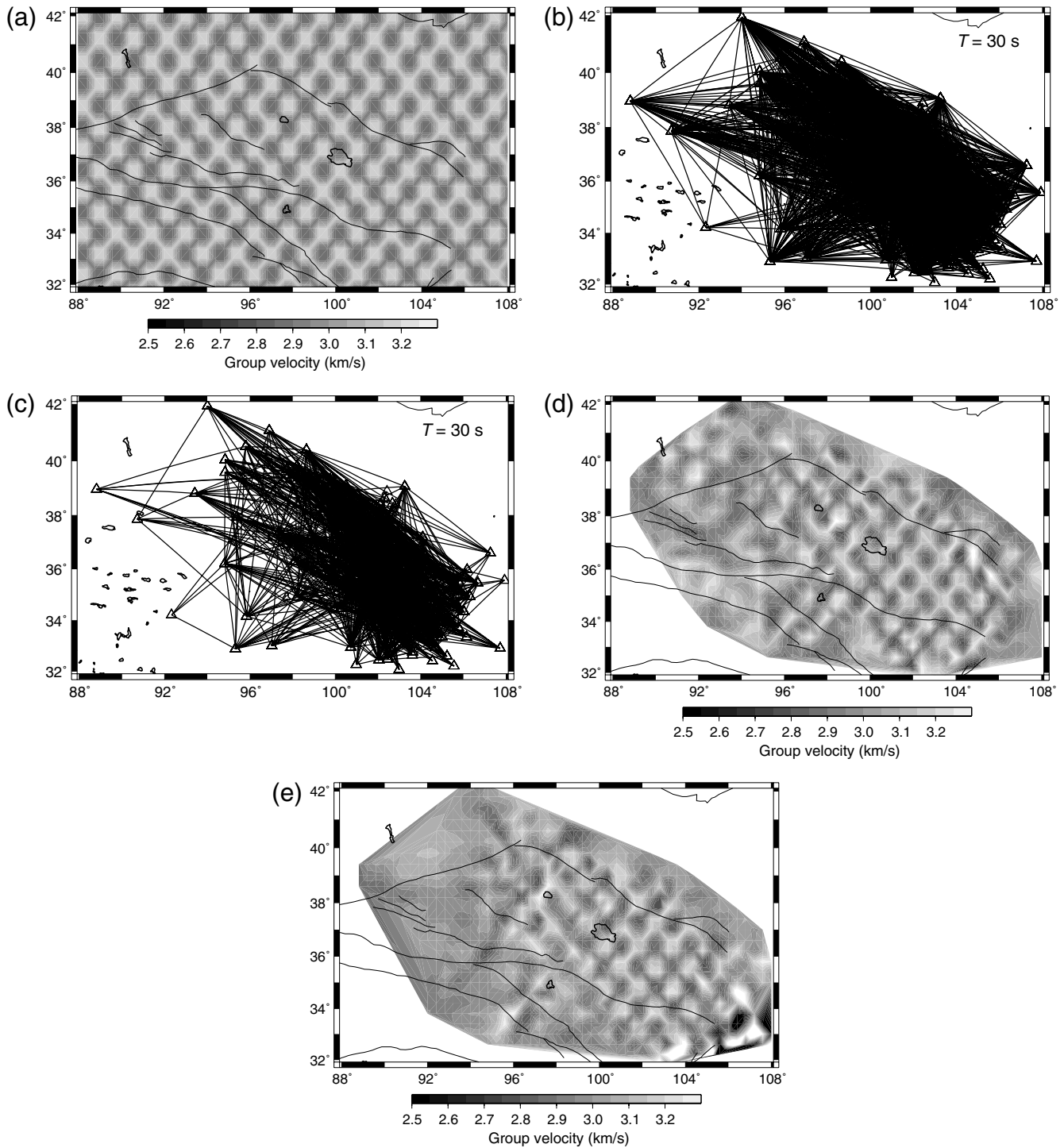
Figure 4. Checkerboard resolution tests with a grid spacing of 0.8°. (a) Theoretical model for $T = 30$ s with disturbing velocities 3.0 ± 0.15 km/s. Path coverage at periods of 30 s for (b) Rayleigh wave and (c) Love wave. Inversion results for (d) Rayleigh wave and (e) Love wave.

supplement to this article). Because surface waves have poor ability to resolve the velocity discontinuity and the trade-off between the shear-wave velocity and Moho depth, we used 10 different initial models by adjusting the shear-wave velocity (Ⓔ Fig. S4, available in the electronic supplement), layer thickness, and Moho depth, then the inversion was repeated

10 times, and the final shear-wave velocity structure was averaged from the 10 inversion solutions.

In our inversion, we adopted an isotropic model to simultaneously fit both Raleigh- and Love-dispersion curves, however, we noticed that for some particular cells showing an LVZ in its mid-to-lower crust, it is hard to fit both
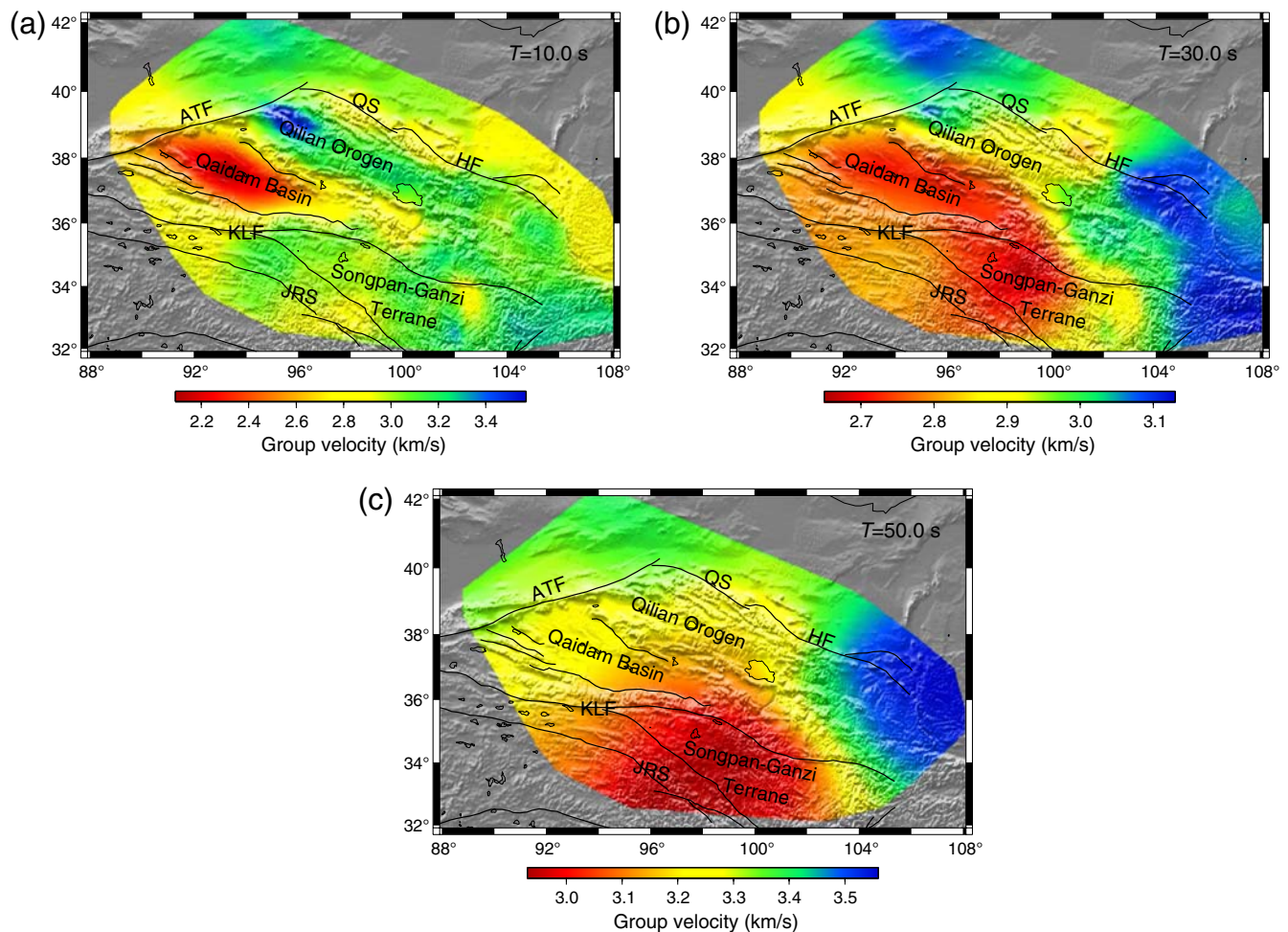
Figure 5.   Estimated Rayleigh-wave group velocity maps at (a) 10 s, (b) 30 s, and (c) 50 s. Period is indicated in the upper right corner of each map. The color version of this figure is available only in the electronic edition.

Rayleigh- and Love-wave dispersion curves, which could relate to the radial anisotropy. Therefore, the obtained S-wave velocity structure in our inversion is somehow the average between V_{Sv} and V_{Sh}. An example of pure path dispersion curves and their corresponding 1D shear-wave velocity models is presented in Figure 7. The location of the grid (104.8° E, 35° N) is identified with a star in Figure 1b. The synthetic dispersion curves for both the Rayleigh and Love waves generally resemble the observed ones well.

The final S-wave velocity structures at depths of 10, 20, 30, and 40 km are shown in Figure 8. The S-wave velocity structure shows significant differences with depth in the study area. Pronounced low shear-wave velocities appear in the Songpan–Ganzi terrane and in the vicinity of the KLF, from the mid-to-lower crust down to at least 40 km (Fig. 8). At 10 km depth, the Qaidam basin is characterized by a low S-wave velocity, and a small patch of very-high-velocity anomaly is observed in the northernmost Qilian orogen (Fig. 8a). Low-velocity anomalies at shallow depth beneath the Qaidam basin could be due to thick sedimentary layers because the Qaidam basin has been in a stable sedimentary environment since Cenozoic time (Chen *et al.*, 1999; Métivier

et al., 1999). At depths of 20 km, the velocity distribution is quite different from velocities at 10 km. The high S-wave velocity appears beneath the Qaidam basin. The upper crust of the Songpan–Ganzi terrane and KLF is characterized by the lowest velocity. Figure 8c shows that at the depth of 30 km, the Qaidam basin is featured with a relatively higher velocity and the Songpan–Ganzi terrane with a lower velocity. We note that relatively lower velocities are observed beneath the north Qilian orogen instead of high velocities at shallow depth (Fig. 8c). The shear-wave velocity map at 40 km depth (Fig. 8d) shows a similar velocity distribution as at the depth of 30 km except that the LVZ beneath the north Qilian orogen is more obvious and becomes larger than that at depth of 30 km. This shear-wave velocity model offers new insights into the subsurface structures beneath the northeast Tibetan plateau, and its implications to the deformation and rise of the Tibetan plateau are discussed in the Discussion section.

Figure 9 presents shear-wave velocity structure along two vertical profiles from the surface down to 70 km depth. In the AA′ profile (Fig. 9a) through the Songpan–Ganzi terrane to the southern Qilian orogen, an evident mid-to-lower crustal LVZ is present only beneath the Songpan–
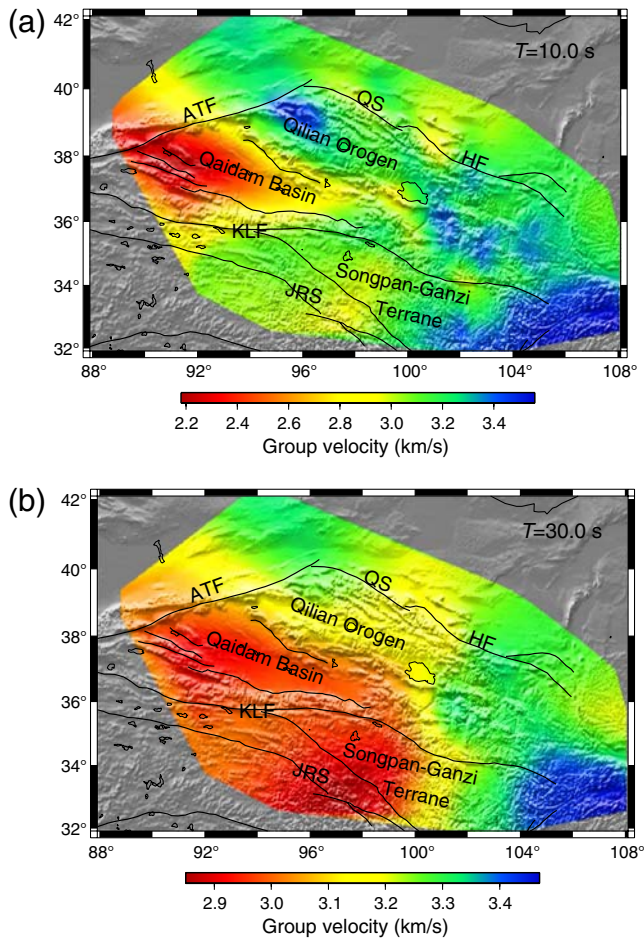
Figure 6. Estimated Love-wave group velocity maps at (a) 10 s and (b) 30 s. Period is indicated in the upper right corner of each map. The color version of this figure is available only in the electronic edition.

Ganzi terrane but not beneath the southern Qilian orogen. In the BB′ profile crossing the Songpan–Ganzi terrane and the northern Qilian orogen (Fig. 9b), an LVZ in the mid-to-lower crust exists beneath the Songpan–Ganzi terrane and the northern Qilian orogen.

Discussion

Generally speaking, our group velocity maps show high correlations with the major tectonic units in the study region. At the same time, both our group velocity maps (Figs. 5 and 6) and shear-wave velocity maps (Fig. 8) reveal significant anomalies within our study area.

Low velocities are clearly observed in the Qaidam basin. However, high velocities are associated with the mountainous areas at short periods (Figs. 5a and 6a) because most mountain regions are mainly dominated by metamorphic rocks (compared with sediment-filled basin). It is well known that seismic velocities of sediments are much lower than those of metamorphic rocks. At 30 s period (Figs. 5b and 6b), the Qaidam basin is still featured with low velocity and shows the influence of
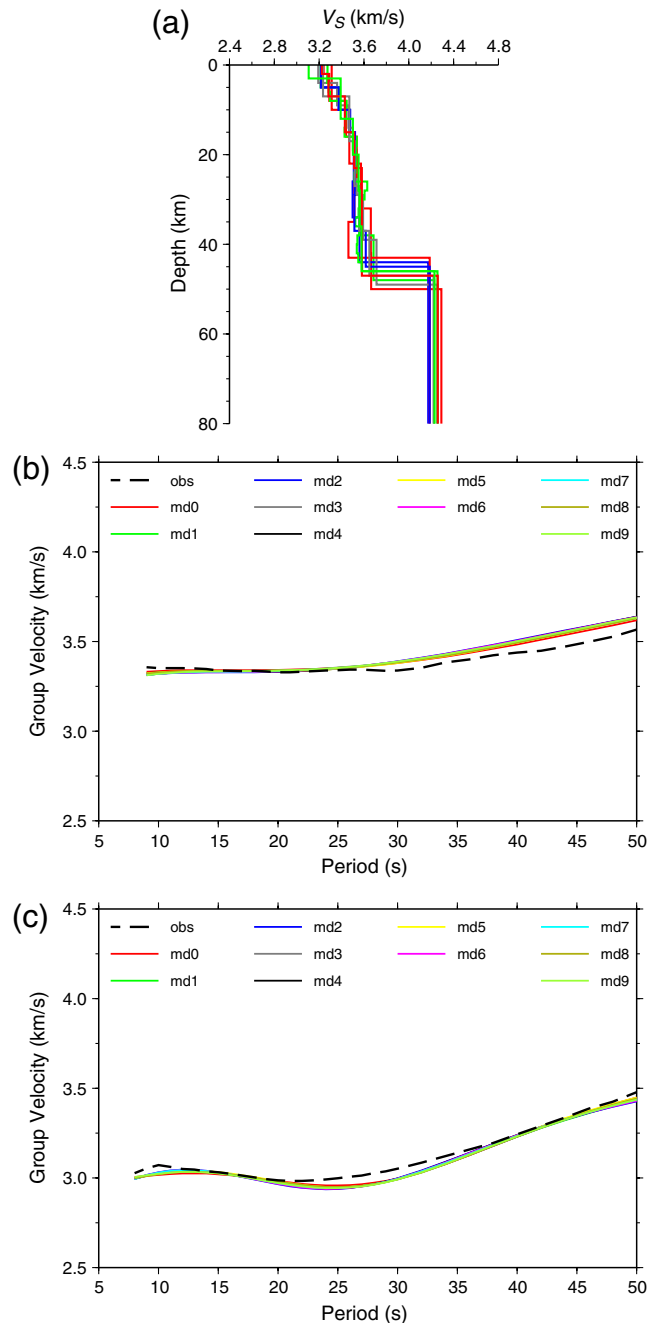

Figure 7. Example of local dispersion curve and the corresponding 1D shear-wave velocity models at the location marked in Figure 1b as the star. (a) The 10 inverted 1D velocity models, (b) the observed (dashed line) and synthetic Love-wave dispersion curves from 10 models, and (c) the observed (dashed line) and synthetic Rayleigh-wave dispersion curves. The color version of this figure is available only in the electronic edition.

sedimentary layers. With the increase of the period, surface-wave energy penetrates the deeper structure of the Earth, so the surface-wave velocities are mainly influenced by the thickness of the crust, as well as the shear velocities in the lower crust and uppermost mantle. For the Love-wave velocity map at 30 s, due to more than 8 km sedimentary cover on average beneath the Qaidam basin, the imprint of the sedimentary
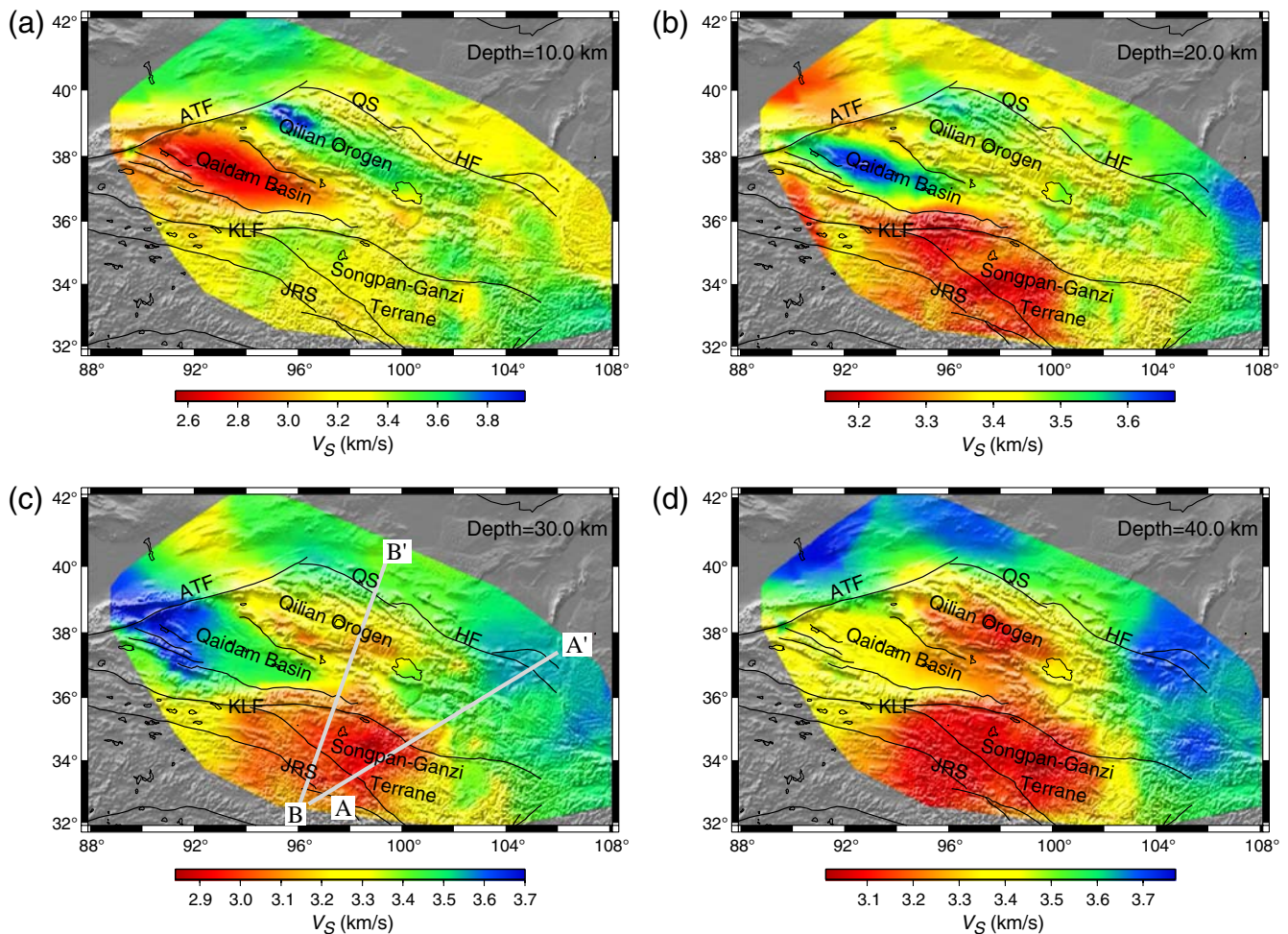
Figure 8. Shear-wave velocity maps at depth (a) 10 km, (b) 20 km, (c) 30 km, and (d) 40 km. Depth is indicated in the upper right corner of each panel. The dark lines show major tectonic features. Lines in (c) delineate the locations of the vertical cross sections shown in Figure 9. The color version of this figure is available only in the electronic edition.

layers still exists; therefore, the velocity map at 30 s is influenced not only by the lower crust, but also by the thick sediments. At the 30 s period, the Songpan–Ganzi terrane shows low velocity due to its thicker crust compared with the basin areas. Rayleigh-wave velocity maps at greater periods (50 s, Fig. 5c) show an inverse correlation with the crustal thickness variation. The Qaidam basin is overall associated with high velocity due to relatively thin crustal thickness in comparison with the mountain areas.

The shear-wave velocity structures derived from both Rayleigh- and Love-wave dispersion curves show that the Songpan–Ganzi terrane is featured with a prominent LVZ in its mid-to-lower crust (~20–40 km), which is consistent with the *P*-velocity model (C. Li *et al.*, 2006) in this area. Meanwhile, as seen in Figures 8 and 9, it is very striking that the northern Qilian orogen associated with a relatively higher topography also features an LVZ in the middle crust, but the LVZ has not been observed beneath the southern Qilian orogen.

What causes such a low-velocity anomaly and the distribution of the mid-to-lower crustal LVZ beneath the Tibetan

plateau are the important questions that need to be discussed. If the lower-crustal velocity were laterally more uniform, this would accentuate the proposed Moho topography (Q. Zhang *et al.*, 2011). The mid-to-lower LVZ beneath the Songpan–Ganzi terrane is similar to the LVZs observed beneath other parts of the plateau, such as the eastern, central, and southern Tibetan plateau. Geophysical studies using different methods also found high-electrical conductivity, high-temperature, partial melting, low-velocity, and low-strength zones in the mid-to-lower crust beneath the plateau (e.g., Clark *et al.*, 2005; Royden *et al.*, 2008; Yao *et al.*, 2008; Guo *et al.*, 2009; Li *et al.*, 2009; Bai *et al.*, 2010; Yang *et al.*, 2012). The crustal flow model suggested that the weak mid-to-lower crustal materials beneath the Tibetan plateau probably contributed to the elevated topography and crustal thickening of the Tibetan plateau (Clark and Royden, 2000; Royden *et al.*, 2008). In their models, they proposed when the crust of adjacent regions is cold and strong, then the weak mid-to-lower crust beneath the plateau could be difficult to flow into adjacent regions, and therefore a narrow and steep plateau margin has been built up. If the crust of adjacent regions is also
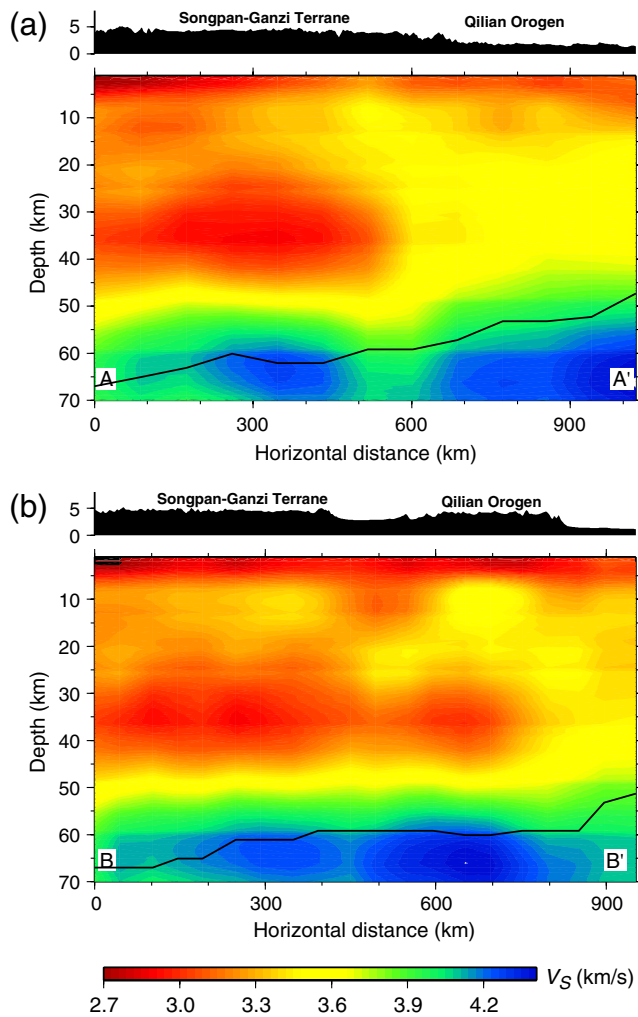
Figure 9. Vertical cross sections of *S*-wave velocity along the profiles AA′ and BB′ shown in Figure 8c. The solid curves are the Moho depth. The color version of this figure is available only in the electronic edition.

weak, then the mid-to-lower crust could escape to regions where crust is weak, thus resulting in a broad and gentle plateau margin with long wavelength and low topographic gradient. Based on their model, in the northeastern plateau margin with a gentle topography gradient, the weak mid-to-lower crustal materials could escape through the Songpan–Ganzi terrane toward the southwestern Ordos platform.

Our results show that a mid-to-lower crustal LVZ has been observed beneath the northern Qilian orogen, with the highest topography and a thickened crust (∼60 km; Yue *et al.*, 2012) compared to its surrounding regions. However, it has not been found beneath the southern Qilian orogen. Because our data have poor resolution in the Qaidam basin, it is hard to evaluate whether the LVZ exists beneath the Qaidam basin and the LVZ beneath the Songpan–Ganzi terrane flows through the Qaidam basin to the northern Qilian orogen. However, our observations in the southern Qilian orogen are probably inconsistent with the simple crustal flow model, in which the eastward moving crust of the central plateau is diverted northeast

and southeast around the Sichuan basin. Therefore, it would support a gentle long-wavelength topographic gradient along the northeastern edge of the Tibetan plateau toward the Ordos platform (Clark *et al.*, 2005; Royden *et al.*, 2008). The lateral distribution of the LVZ beneath the northern Qilian orogen shows a very good correlation with the area of thickened crust and highest topography. As a result of the continent–continent collision, the main part of the Tibetan plateau was uplifted and has a very thick crust, and the mid-crustal LVZ is widely distributed in the main plateau. Therefore, we infer that the mid-to-lower crustal LVZ beneath the northwestern Qilian orogen may be attributed to the crustal thickening and surface uplift responding to the ongoing collision of the plateau, which is similar to that of the main part of the Tibetan plateau; however, at this point, it could be difficult to use our results to support the crustal flow mode.

Conclusion

In this study, we obtained group velocity maps of Rayleigh and Love waves in the northeast Tibetan plateau using broadband seismic data recorded by temporary broadband seismic arrays and the regional seismic networks. Cross-correlation functions are computed in one-hour segments, and group velocity dispersion curves are determined using the multiple-filter analysis technique. The large variation of velocity structure indicates strong heterogeneities and structure complexities in the study area. Prominent low-velocity layers have been found in the mid-to-lower crust beneath the Songpan–Ganze terrane and the northern Qilian orogen. The LVZ beneath the northern Qilian orogen may be attributed to the crustal thickening and surface uplift, which is responding to the ongoing collision. From this study, there is no clear evidence of the low-velocity mid-to-lower crust beneath the southern Qilian orogen as the crustal flow model predicts.

Data and Resources

Acknowledgments

References

Arnaud, N. O., Ph. Vidal, P. Tapponnier, Ph. Matte, and W. Deng (1992). The high K₂O volcanism of northwestern Tibet: Geochemistry and tectonic implications, *Earth Planet. Sci. Lett.* **111,** 351–367.

Bai, D., M. J. Unsworth, M. A. Meju, X. Ma, J. Teng, X. Kong, Y. Sun, J. Sun, L. Wang, C. Jiang, C. Zhao, P. Xiao, and M. Liu (2010). Crustal deformation of the eastern Tibetan plateau revealed by magnetotelluric imaging, *Nature Geosci.* **3,** 358–362.

Bendick, R., and L. Flesch (2007). Reconciling lithospheric deformation and lower crustal flow beneath central Tibet, *Geology* **35,** 895–898, doi: 10.1130/G23714A.1.

Brown, L. D., W. Zhao, K. D. Nelson, M. Hauck, D. Alsdorf, A. Ross, M. Cogan, M. Clark, X. Liu, and J. Che (1996). Bright spots, structure, and magmatism in southern Tibet from INDEPTH seismic reflection profiling, *Science* **274,** 1688–1690.

Chen, W., C. Chen, and J. L. Nabelek (1999). Present-day deformation of the Qaidam basin with implications for intra-continental tectonics, *Tectonophysics* **305,** 165–181.

Chung, S., M. Chu, Y. Zhang, Y. Xie, C. Lo, T. Lee, C. Lan, X. Li, Q. Zhang, and Y. Wang (2005). Tibetan tectonic evolution inferred from spatial and temporal variations in post-collisional Magmatism, *Earth Sci. Rev.* **68,** 73–196.

Clark, M., and L. Royden (2000). Topographic ooze: Building the eastern margin of Tibet by lower crustal flow, *Geology* **28,** 703–706.

Clark, M., J. Bush, and L. Royden (2005). Dynamic topography produced by lower crustal flow against rheological strength heterogeneities bordering the Tibetan plateau, *Geophys. J. Int.* **162,** 575–590.

Constable, S., R. Parker, and C. Constable (1987). Occam's inversion: A practical algorithm for generating smooth models from electromagnetic sounding data, *Geophysics* **52,** 289–300.

Dai, J., C. Wang, R. Hebert, Y. Li, H. Zhong, R. Guillaume, R. Bezard, and Y. Wei (2011). Late Devonian OIB alkaline gabbro in the Yarlung Zangbo suture zone: Remnants of the Paleo-Tethys? *Gondwana Research*, Special Section: The South and East Facades of Sundaland **19,** no. 1, 232–243, doi: 10.1016/j.gr.2010.05.015.

DeGroot-Hedlin, C., and S. Constable (1990). Occam's inversion to generate smooth, two dimensional models from magnetotelluric data, *Geophysics* **55,** no. 12, 1613–1624.

Deng, W. (1997). Cenozoic volcanism and lithosphere tectonic evolution in the northern Tibetan plateau, China, in *Igneous Petrology*, Z. Li, J. Qi, and Z. Zhang (Editors), Vol. 15, 30th International Geological Congress, Utrecht, The Netherlands, Tokyo, Japan, 3–12.

Dziewonski, A., S. Block, and M. Landisman (1969). A technique for the analysis of transient seismic signals, *Bull. Seismol. Soc. Am.* **59,** 427–444.

Guo, Z., X. Gao, H. Yao, J. Li, and W. Wang (2009). Midcrustal low-velocity layer beneath the central Himalaya and southern Tibet revealed by ambient noise array tomography, *Geochem. Geophys. Geosyst.* **10,** Q05007, doi: 10.1029/2009GC002458.

Herrmann, R. B. (1973). Some aspects of band-pass filtering of surface waves, *Bull. Seismol. Soc. Am.* **63,** no. 2, 663–671.

Herrmann, R. B., and C. J. Ammon (2004). Surface waves, receiver functions and crustal structure, *Computer Programs in Seismology*, Version 3.30, Saint Louis University, Missouri.

Huang, W., J. Ni, F. Tilmann, D. Nelson, J. Guo, W. Zhao, J. Mechie, R. Kind, J. Saul, R. Rapine, and T. Hearn (2000). Seismic polarization anisotropy beneath the central Tibet plateau, *J. Geophys. Res.* **105,** 27979–27989.

Huang, Z., W. Su, Y. Peng, Y. Zheng, and H. Li (2003). Rayleigh wave tomography of China and adjacent regions, *J. Geophys. Res.* **108,** no. B2, 2073, doi: 10.1029/2001JB001696.

Karplus, M. S., S. L. Klemperer, J. F. Lawrence, W. Zhao, J. Mechie, F. Tilmann, E. Sandvol, and J. Ni (2013). Ambient-noise tomography of north Tibet limits geological terrane signature to upper-middle crust, *Geophys. Res. Lett.* **40,** no. 5, 808–813, doi: 10.1002/grl.50202.

Karplus, M. S., W. Zhao, S. L. Klemperer, Z. Wu, J. Mechie, D. Shi, L. D. Brown, and C. Chen (2011). Injection of Tibetan crust beneath the south Qaidam basin: Evidence from INDEPTH IV wide-angle seismic data, *J. Geophys. Res.* **116,** B07301, doi: 10.1029/2010JB007911.

Kind, R., J. Ni, W. Zhao, J. Wu, X. Yuan, L. Zhao, E. Sandvol, C. Reese, J. Nabelek, and T. Hearn (1996). Evidence from earthquake data for a partially molten crustal layer in southern Tibet, *Science* **274,** 1692–1694.

Kind, R., X. Yuan, J. Saul, D. Nelson, S. V. Sobolev, J. Mechie, W. Zhao, G. Kosarev, J. Ni, U. Achauer, and M. Jiang (2002). Seismic images of crust and upper mantle beneath Tibet: Evidence for Eurasian plate subduction, *Science* **298,** no. 5596, 1219–1221.

Li, C., R. van der Hilst, and M. Toksöz (2006). Constraining *P*-wave velocity variations in the upper mantle beneath southeast Asia, *Phys. Earth Planet. In.* **154,** no. 2, 180–195.

Li, H., F. Bernardi, and A. Michelini (2010). Surface wave dispersion measurements from ambient seismic noise analysis in Italy, *Geophys. J. Int.* **180,** no. 3, 1242–1252, doi: 10.1111/j.1365-246X.2009.04476.x.

Li, H., S. Li, X. Song, M. Gong, X. Li, and J. Jia (2012). Crustal and uppermost mantle velocity structure beneath northwestern China from seismic ambient noise tomography, *Geophys. J. Int.* **188,** no. 1, 131–143, doi: 10.1111/j.1365-246X.2011.05205.x.

Li, H., W. Su, C. Wang, and Z. Huang (2009). Ambient noise Rayleigh wave tomography in western Sichuan and eastern Tibet, *Earth Planet. Sci. Lett.* **282,** nos. 1/4, 201–211.

Li, H., W. Su, C. Wang, Z. Huang, and Z. Lv (2010). Ambient noise Love wave tomography in the eastern margin of the Tibetan plateau, *Tectonophysics* **491,** nos. 1/4, 194–204, doi: 10.1016/j.tecto.2009.12.018.

Li, S., D. Walter, and J. Fan (2006). Crustal structure of mainland China from deep seismic sounding data, *Tectonophysics* **420,** no. 12, 239–252.

Maceira, M., S. R. Taylor, C. J. Ammon, X. Yang, and A. A. Velasco (2005). High-resolution Rayleigh wave slowness tomography of central Asia, *J. Geophys. Res.* **110,** B06304, doi: 10.1029/2004JB003429.

Métivier, F., Y. Gaudemer, P. Tapponnier, and M. Klein (1999). Mass accumulation rates in Asia during the Cenozoic, *Geophys. J. Int.* **137,** no. 2, 280–318.

Molnar, P., and P. Tapponnier (1975). Cenozoic tectonics of Asia: Effects of a continental collision, *Science* **189,** no. 4201, 419–426.

Molnar, P., P. England, and J. Martinod (1993). Mantle dynamics, uplift of the Tibetan plateau and the Indian Monsoon, *Rev. Geophys.* **31,** no. 4, 357–396.

Nelson, K. D., W. Zhao, L. D. Brown, J. Kuo, J. Chen, X. Liu, S. L. Klemperer, Y. Makovsky, R. Meissner, J. Mechie *et al.* (1996). Partially molten middle crust beneath southern Tibet: Synthesis of project INDEPTH results, *Science* **274,** 1684–1688.

Owens, T., and G. Zandt (1997). Implications of crustal property variations for models of Tibetan plateau evolution, *Nature* **387,** 37–43.

Pan, S., and F. Niu (2011). Large contrasts in crustal structure and composition between the Ordos plateau and the NE Tibetan plateau from receiver function analysis, *Earth Planet. Sci. Lett.* **303,** nos. 3/4, 291–298.

Pearce, J., and H. Mei (1988). Volcanic rocks of the 1985 Tibet geotraverse: Lhasa to Golmud, *Phil. Trans. Roy. Soc. London* **327,** no. 1594, 169–201.

Powell, C., and P. Conaghan (1975). Tectonic models of the Tibetan plateau, *Geology* **3,** no. 12, 727–731.

Royden, L. H., B. C. Burchfiel, R. W. King, E. Wang, Z. Chen, F. Shen, and Y. Liu (1997). Surface deformation and lower crustal flow in eastern Tibet, *Science* **276,** no. 5313, 788–790.

Royden, L. H., B. C. Burchfiel, and R. van der Hilst (2008). The geological evolution of the Tibetan plateau, *Science* **321,** no. 5892, 1054–1058.

Shen, Y., D. Shi, X. Li, E. Sandvol, A. Li, Z. Zhang, H. Li, and X. Liang (2008). Initial report on the northeastern Tibetan plateau seismic experiment and study of the May 12, 2008, Wenchuan earthquake, *Eos Trans. AGU* **89,** no. 53 (Fall Meet. Suppl.), Abstract U23B-66.

Tapponnier, P., and P. Molnar (1977). Active faulting and tectonics in China, *J. Geophys. Res.* **82,** no. 20, 2905–2930.

Tapponnier, P., Z. Xu, F. Roger, B. Meyer, N. Arnaud, G. Wittlinger, and J. Yang (2001). Oblique stepwise rise and growth of the Tibet plateau, *Science* **294,** no. 5547, 1671–1677.

Tilmann, F., J. Ni, and INDEPTH Seismic Team (2003). Seismic imaging of the downwelling Indian lithosphere beneath central Tibet, *Science* **300,** 1424–1427.

Unsworth, M., A. Jones, W. Wei, G. Marquis, S. Gokarn, and J. Spratt (2005). Crustal rheology of the Himalaya and southern Tibet from magnetotelluric data, *Nature* **438,** 78–81.

Vergne, J., G. Wittlinger, V. Farra, and H. Su (2003). Evidence for upper crustal anisotropy in the Songpan–Ganze (northeastern Tibet) terrane, *Geophys. Res. Lett.* **30,** no. 11, 1552–1555, doi: 10.1029/2002GL016847.

Vergne, J., G. Wittlinger, H. Qian, P. Tapponnier, G. Poupinet, M. Jiang, G. Herquel, and A. Paul (2002). Seismic evidence for stepwise thickening of the crust across the NE Tibetan plateau, *Earth Planet. Sci. Lett.* **203,** no. 1, 25–53.

Wang, C., W. Chan, and W. D. Mooney (2003). Three-dimensional velocity structure of crust and upper mantle in southwestern China and its tectonic implications, *J. Geophys. Res.* **108,** no. B9, 176–193, doi: 10.1029/2002JB001973.

Wang, C., W. Han, J. Wu, H. Lou, and W. Chan (2007). Crustal structure beneath the eastern margin of the Tibetan plateau and its tectonic implications, *J. Geophys. Res.* **112,** no. B07307, doi: 10.1029/2005JB003873.

Wang, Q., P. Zhang, J. T. Freymueller, R. Bilham, K. M. Larson, X. Lai, X. You, Z. Niu, J. Wu, Y. Li, J. Liu, Z. Yang, and Q. Chen (2001). Present-day crustal deformation in China constrained by global positioning system measurements, *Science* **294,** no. 5542, 574–577.

Wei, W., M. Unsworth, A. Jones, J. Booker, H. Tan, D. Nelson, L. Chen, S. Li, K. Solon, P. Bedrosian, S. Jin, M. Deng, J. Ledo, D. Kay, and B. Roberts (2001). Detection of widespread fluids in the Tibetan crust by magnetotelluric studies, *Science* **292,** 716–718.

Wessel, P., and W. H. F. Smith (1998). New, improved version of the generic mapping tools released, *Eos Trans. AGU* **79,** no. 47, 579, doi: 10.1029/98EO00426.

Wittlinger, G., F. Masson, G. Poupinet, P. Tapponnier, M. Jiang, G. Herquel, J. Guilbert, U. Achauer, G. Xue, and D. Shi (1996). Seismic tomography of northern Tibet and Kunlun: Evidence for crustal blocks and mantle velocity contrasts, *Earth Planet. Sci. Lett.* **139,** 263–279, doi: 10.1016/0012-821X(95)00235-5.

Xu, Y., F. Liu, J. Liu, and H. Chen (2002). Crust and upper mantle structure beneath western China from P wave travel time tomography, *J. Geophys. Res.* **107,** 2220, doi: 10.1029/2001JB000402.

Xu, Z. (1992). *Orogenic Processes of the Songpan–Ganze Orogenic Belt of China*, Geol. Press, Beijing, 1–190 (in Chinese).

Yang, Y., M. H. Ritzwoller, Y. Zheng, W. Shen, A. Levshin, and Z. Xie (2012). A synoptic view of the distribution and connectivity of the mid-crustal low velocity zone beneath Tibet, *J. Geophys. Res.* **117,** no. B04303, doi: 10.1029/2011JB008810.

Yao, H., C. Beghein, and R. D. Van der Hilst (2008). Surface wave array tomography in SE Tibet from ambient seismic noise and two-station analysis:-II. Crustal and upper-mantle structure, *Geophys. J. Int.* **173,** 205–219, doi: 10.1111/j.1365-246X.2007.03696.x.

Yin, A., and T. M. Harrison (2000). Geologic evolution of the Himalayan-Tibetan orogeny, *Annu. Rev. Earth Planet. Sci.* **28,** 211–280.

Yue, H., J. Chen, E. Sandvol, J. Ni, T. Hearn, S. Zhou, Y. Feng, Z. Ge, A. Trujillo, Y. Wang, G. Jin, M. Jiang, Y. Tang, X. Liang, S. Wei, H. Wang, and W. Fan (2012). Lithospheric and upper mantle structure of the northeastern Tibetan plateau, *J. Geophys. Res.* **117,** no. B04303, doi: 10.1029/2011JB008545.

Zhang, C., D. Yang, H. Wang, Y. Takahashi, and H. Ye (2010). Neoproterozoic mafic-ultramafic layered intrusion in Quruqtagh of northeastern Tarim block, NW China: Two phases of mafic igneous activity with different mantle resources, *Gondwana Res.* **19,** no. 1, 177–190, doi: 10.1016/j.gr.2010.03.012.

Zhang, P., Z. Shen, M. Wang, W. Gan, R. Burgmann, P. Molnar, Q. Wang, Z. Niu, J. Sun, J. Wu, H. Sun, and X. You (2004). Continous deformation of the Tibetan plateau from Global Positioning System data, *Geology* **32,** no. 9, 809–812.

Zhang, Q., E. Sandvol, J. Ni, Y. Yang, and Y. Chen (2011). Rayleigh wave tomography of the northeastern margin of the Tibetan plateau, *Earth Planet. Sci. Lett.* **304,** nos. 1/2, 103–112, doi: 10.1016/j.epsl.2011.01.021.

Zhang, Z., S. Klemperer, Z. Bai, Y. Chen, and J. Teng (2011). Crustal structure of the Paleozoic Kunlun orogeny from an active-source seismic profile between Moba and Guide in East Tibet, China, *Gondwana Res.* **19,** no. 4, 994–1007, doi: 10.1016/j.gr.2010.09.008.

Zhang, Z., X. Yuan, Y. Chen, X. Tian, R. Kind, and X. Li (2010). Seismic signature of the collision between the East Tibetan escape flow and the Sichuan basin, *Earth Planet. Sci. Lett.* **292,** no. 3/4, 254–264.

Zhao, J., Q. Deng, and Z. Lu (2004). A review of the geophysical exploration studies on northwest China, in *Progress in Seismological and Solid Earth Geophysical Researches in Mainland China*, Y. T. Chen, J. W. Teng, R. Kan, and C. Y. Wang (Editors), Seismological Press, Beijing, 128–134 (in Chinese).

Zhao, W., and W. J. Morgan (1985). Uplift of Tibetan plateau, *Tectonics* **4,** no. 4, 359–369.

Zhu, L., and D. V. Helmberger (1998). Moho offset across the northern margin of the Tibetan plateau, *Science* **281,** 1170–1172.

Key Laboratory of Geo-detection (China University of Geosciences)
Ministry of Education
Beijing 100083, China
xinfuli@cugb.edu.cn
lih@cugb.edu.cn
    (X.L., H.L.)

Graduate School of Oceanography
University of Rhode Island
Narragansett, Rhode Island 02882
yshen@gso.uri.edu
    (Y.S.)

Seismological Bureau of Heibei Province
Shijiazhuang 050021, China
gongm@eq-he.ac.cn
    (M.G.)

Institute of Mineral Resources
Chinese Academy of Geological Sciences
26 Baiwanzhuang Road
Beijing 100037, China
shidanian@cags.net.cn
    (D.S.)

Department of Geological Sciences
University of Missouri
Columbia, Missouri 65211
sandvole@missouri.edu
    (E.S.)

Earth and Atmospheric Sciences Department
University of Houston
Houston, Texas 77204-5007
ali2@mail.uh.edu
    (A.L.)